# Effects of Interfacial Lattice Mismatching on Wetting of Ni-Plated Steel by Magnesium

ALI M. NASIRI, MOK Y. LEE, DAVID C. WECKMAN, and Y. ZHOU

In this study, wetting has been characterized by measuring the contact angles of AZ92 Mg alloy on Ni-electroplated steel as a function of temperature. Reactions between molten Mg and Ni led to a contact angle of about 86 deg in the temperature range of 891 K to 1023 K (618 °C to 750 °C) (denoted as Mode I) and a dramatic decrease to about 46 deg in the temperature range of 1097 K to 1293 K (824 °C to 1020 °C) (denoted as Mode II). Scanning and transmission electron microscopy (SEM and TEM) indicated that AlNi + $Mg_2Ni$ reaction products were produced between Mg and steel (Mg-AlNi-$Mg_2Ni$-Ni-Fe) in Mode I, and just AlNi between Mg and steel (Mg-AlNi-Fe) in Mode II. From high resolution TEM analysis, the measured interplanar mismatches for different formed interfaces in Modes I and II were 17 $\text{pct}_{\{10\bar{1}1\}_{Mg}//\{110\}_{AlNi}}$-104.3 $\text{pct}_{\{110\}_{AlNi}//\{10\bar{1}0\}_{Mg_2Ni}}$-114 $\text{pct}_{\{0003\}_{Mg_2Ni}//\{111\}_{Ni}}$ and 18 $\text{pct}_{\{10\bar{1}1\}_{Mg}//\{110\}_{AlNi}}$-5 $\text{pct}_{\{110\}_{AlNi}//\{110\}_{Fe}}$, respectively. An edge-to-edge crystallographic model analysis confirmed that $Mg_2Ni$ produced larger lattice mismatching between interfaces with calculated minimum interplanar mismatches of 16.4 $\text{pct}_{\{10\bar{1}1\}_{Mg}//\{110\}_{AlNi}}$-108.3 $\text{pct}_{\{110\}_{AlNi}//\{10\bar{1}1\}_{Mg_2Ni}}$-17.2 $\text{pct}_{\{10\bar{1}1\}_{Mg_2Ni}//\{100\}_{Ni}}$ for Mode I and 16.4 $\text{pct}_{\{10\bar{1}1\}_{Mg}//\{110\}_{AlNi}}$-0.6 $\text{pct}_{\{111\}_{AlNi}//\{111\}_{Fe}}$ for Mode II. Therefore, it is suggested that the poor wettability in Mode I was caused by the existence of $Mg_2Ni$ since AlNi was the immediate layer contacting molten Mg in both Modes I and II, and the presence of $Mg_2Ni$ increases the interfacial strain energy of the system. This study has clearly demonstrated that the lattice mismatching at the interfaces between reaction product(s) and substrate, which are not in direct contact with the liquid, can greatly influence the wetting of the liquid.

DOI: 10.1007/s11661-014-2514-8


## I. INTRODUCTION

A comprehensive study of the factors responsible for the wetting of a solid by a liquid metal is not only of scientific interest, but also of significant technological importance. This information is particularly valuable for many metallurgical processes, for instance fabrication of metal-ceramic composites, thin film materials, hot dip metallic coating of steel, soldering in microelectronics, and brazing processes.[1]

It is well known that wettability of a solid by a liquid is affected by numerous factors, such as solubility, reactivity, temperature, working atmosphere, impurities, substrate surface conditions including adsorption, roughness, crystallographic orientation, *etc*.[2] In reactive systems, where extensive dissolution and reaction may occur at the solid-liquid interface,[3] the steady contact angle between solid and liquid is nearly equal to the contact angle of the liquid on the reaction product itself; the generally accepted reactive wetting mechanism in metallic-metallic systems.[4–6] As a result, the final contact angle is given by applying Young's equation to the liquid-reaction product-vapor system instead of liquid-solid substrate-vapor.[4] Therefore, it has been accepted that the liquid-reaction product interfacial energy has a dominant effect on wetting. The effects of other factors, such as the reaction product-substrate interfacial energy or other reaction products which are not in direct contact with the liquid phase have not yet been studied. An example which highlights weakness of the reactive wetting mechanism proposed above is the wetting of Sn-3Ag-*x*Bi solders on Fe-42Ni alloy-substrate studied by Saiz *et al*.[7] Their results showed different contact angles of 57 and 77 deg when the temperature was 523 K and 723 K (250 °C and 450 °C), respectively. Moreover, they showed different reaction product(s), which was Fe (substrate)-$FeSn_2$ (reaction product)-Sn (solder) at 523 K (250 °C) and Fe-FeSn-$FeSn_2$-Sn at 723 K (450 °C). However, the underlying mechanism behind varying contact angles was not provided and cannot be simply explained using the proposed mechanism for reactive wetting in metallic-metallic system, since the immediate reaction product in contact with Sn solder was $FeSn_2$ in both cases.

The formation of the reaction product(s) is associated with the formation of new interfaces. Due to different

ALI M. NASIRI, Postdoctoral Fellow, is with the Centre for Advanced Materials Joining, University of Waterloo, Waterloo, ON, N2L 3G1, Canada. Contact e-mail: amnasiri@uwaterloo.ca MOK Y. LEE, Senior Researcher, is with the Centre for Advanced Materials Joining, University of Waterloo, and also with the System Solution Research Center, Research Institute of Industrial Science & Technology, 67 Cheongam-Ro, Pohang, 790-330, Korea. DAVID C. WECKMAN and Y. ZHOU, Professors, are with the Department of Mechanical & Mechatronics Engineering, Centre for Advanced Materials Joining, University of Waterloo.

Manuscript submitted May 26, 2014.
Article published online August 26, 2014

lattice parameters between the substrate and reaction product or the reaction product and the solidified region, an intrinsic strain in the reaction product arises. The magnitude of this extensional strain is proportional to the lattice mismatch between the reaction product and the substrate ($\varepsilon_0 = \frac{d_S - d_R}{d_S}$, where $d_S$ and $d_R$ are the lattice parameters of the substrate and reaction product, respectively).[8] If the thickness of reaction product is very small compared to the substrate thickness, then the elastic mismatch is entirely distributed into the reaction product.[8]

The free (strain) energy density, $E_\varepsilon$, associated with isothermal linear-elastic straining of a crystalline reaction product (as given by Hooke's law) is[9]:

$$E_\varepsilon = \frac{\mu}{1-\nu}\varepsilon_0^2 f^2(y) \qquad [1]$$

where $\mu$ and $\nu$ are shear modulus and Poisson's ratio of the reaction product, respectively, and $f(y)$ is the unit step function. Therefore, the strain energy is always positive, and proportional to the square of the strain. This strain energy will increase the total interfacial energy. As a result, the total free energy needed to overcome the wetting barrier increases. In such a way, the interfacial energy and wetting can be dependent on the crystallographic dis-registry and lattice matching between the reaction product(s) and the substrate. However, no detailed study on the effect of the lattice matching on wettability in multi-component metallic systems has been reported.

There is a need for an in-depth investigation into the molten magnesium alloy-steel interface utilizing detailed and well-controlled wetting experiments. This need arises due to the non-existence of studies on the fundamental mechanisms and reaction characteristics at play during the reactive wetting of steels by molten magnesium alloys. Typically, magnesium does not wet or bond to steel[10] because of the nearly zero solubility of magnesium in iron. Wetting can, however, be improved in immiscible alloy systems using an interlayer and forming a continuous layer of new solid compound (reaction product) at the interface.[11] In this article a reactive system including Ni-electroplated steel and AZ92 Mg alloy (liquid) using a laser as the heat source is studied to understand the effect of reaction products, especially lattice matching between formed interfacial phase(s) and substrate on wettability in a strong interaction metallic-metallic system. This study has clearly demonstrated that the lattice mismatching at the interfaces between reaction product(s) and substrate, which are not in direct contact with liquid phase, can greatly influence the wetting of the liquid.

### A. *Experimental Procedure*

Spreading of a homogeneous alloy droplet can be performed in a fully isothermal conditions using transferred drop[12] or dispensed drop[13] types of sessile drop techniques. However, these isothermal conditions differ from real practical applications which have inherent non-equilibrium thermodynamic conditions. Laser brazing of Ni-electroplated steel to AZ31B magnesium sheet using AZ92 Mg alloy filler metal, studied by Nasiri *et al.*,[14] showed different wetting behaviors at the bottom and the top side of a single flare bevel lap joint. In their study, formation of different reaction products, *i.e.*, AlNi + $Mg_2Ni$ and AlNi at the bottom and the top side of the joint interface, respectively, were reported.[14] For further analysis, in the current study, wetting experiments were performed using the classic version of the sessile drop technique in which a piece of the AZ92 Mg alloy was placed on the steel substrate and the system was heated to the experimental temperature. In order to simulate and characterize the wetting behavior close to the laser brazing conditions, a diode laser was used to heat up and melt the Mg alloy.

**Table I. Measured Chemical Composition of the Steel Sheet and TiBraze Mg 600 Brazing Alloy (Weight Percent)**

| | Al | Zn | Mn | C | Fe | Mg |
|---|---|---|---|---|---|---|
| Steel | — | — | 0.5 | 0.01 | bal. | — |
| TiBraze Mg 600 | 9.05 | 1.80 | 0.18 | — | — | bal. |

In the present study, 30 × 40 mm samples were cut from 0.25 mm thick Ni-electroplated steel sheet and used as the substrate. The Ni coating layer on the steel sheet was 5 $\mu$m thick. A 5 mm length of Mg alloy (2.4 mm diameter around 0.3 g) specimen was cut and the oxide layer on the surface of the specimen was cleaned by grinding using SiC abrasive paper. The chemical compositions of the steel sheet and the Mg alloy are given in Table I. All specimens were ultrasonically cleaned in acetone to remove oil and other contaminants from the specimen surfaces. The Mg alloy specimen was then placed in the middle of the steel substrate as shown in Figure 1. The flux used in the experiments was commercially named as Superior No. 21 manufactured by Superior Flux and Mfg. Company, which is a powder flux composed of LiCl (35 to 40 wt pct), KCl (30 to 35 wt pct), NaF (10 to 25 wt pct), NaCl (8 to 13 wt pct), and $ZnCl_2$ (6 to 10 wt pct).[15] The flux provided enough shielding during the wetting test; therefore, a shielding gas was not necessary.

The wettability test was performed using the Nuvonyx diode laser system with a maximum power of 4.0 kW. To obtain a laser beam intensity distribution all over the Mg alloy, 30 mm defocusing of the laser beam was applied. The diode laser beam was used for 1.6 s to melt the Mg alloy specimen on the substrate using different laser powers. Also, to measure the temperature profile *vs* time at different process parameters a thermocouple was attached to the bottom at the center of the steel substrate (see Figure 1).

Each test was repeated five times. After each test, the flux was washed off immediately using hot water. The samples were cross-sectioned using a high speed wafer cutting machine and mounted in epoxy. The mounted samples were ground and polished with silicon carbide-coated papers and diamond suspension, respectively. The cross-sectioned samples were photographed and the

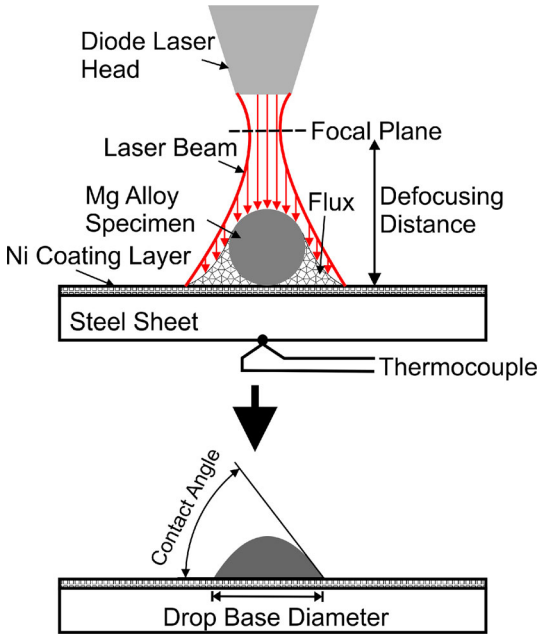


Fig. 1—Schematic of the wetting test.

contact angles were measured using CorelDRAW software.

The macrostructure of sample cross-sections produced for the contact angle variation measurements and the microstructure and compositional analysis were determined using a JEOL JSM-6460 SEM equipped with an Oxford INCA energy dispersive X-ray spectrometer (EDS). For TEM analysis of the Mg alloy-steel interface, TEM foils were prepared using the focused ion beam (FIB) (Zeiss NVision 40 [Carl Zeiss, Chicago, IL] FIB/field emission-SEM) and an in situ lift-out technique.[16] A carbon coating was deposited prior to FIB milling to protect the sample surface and the area of interest upon exposure to the $Ga^+$ beam. Once the TEM foil was attached to a Cu grid, final thinning was performed on the lamella, initially at an acceleration voltage of 30 kV, and finally at a low voltage of 1 kV because the milling of the Mg-Al fusion zone is much faster than that of Ni-plated steel substrate. Details of this procedure can be found in Reference 16. The Mg alloy-substrate interface was observed with a JEOL JEM-2010F field emission transmission electron microscope operated at 200 kV.

## II. RESULTS AND DISCUSSION

The laser power directly affects the peak temperature during wettability tests in the range between 891 K (618 °C) [higher than liquidus temperature of the Mg alloy and flux activation temperature ≈873 K (600 °C)] upto 1293 K (1020 °C) [close to the boiling point temperature of magnesium ≈ 1373 K (1100 °C)]. The selected laser powers, together with the maximum measured temperature at each power, and the measured contact angle after solidification for each specimen are reported in Table II.

**Table II. Wetting Test Parameters Showing the Maximum Temperatures and the Contact Angles**

| Power (kW) | Average of $T_{Max.}$ [K (°C)] | Average of Contact Angle (deg) |
|---|---|---|
| 0.72 | 890.7 (617.7) | 88.0 |
| 0.76 | 928 (655) | 86.6 |
| 0.8 | 973.2 (700.2) | 85.2 |
| 0.84 | 1023.4 (750.4) | 85.1 |
| 0.88 | 1096.8 (823.8) | 46.8 |
| 0.92 | 1124.6 (851.6) | 46.5 |
| 0.96 | 1160.7 (887.7) | 46.4 |
| 1.00 | 1213.2 (940.2) | 45.4 |
| 1.04 | 1292.9 (1019.9) | 45.2 |

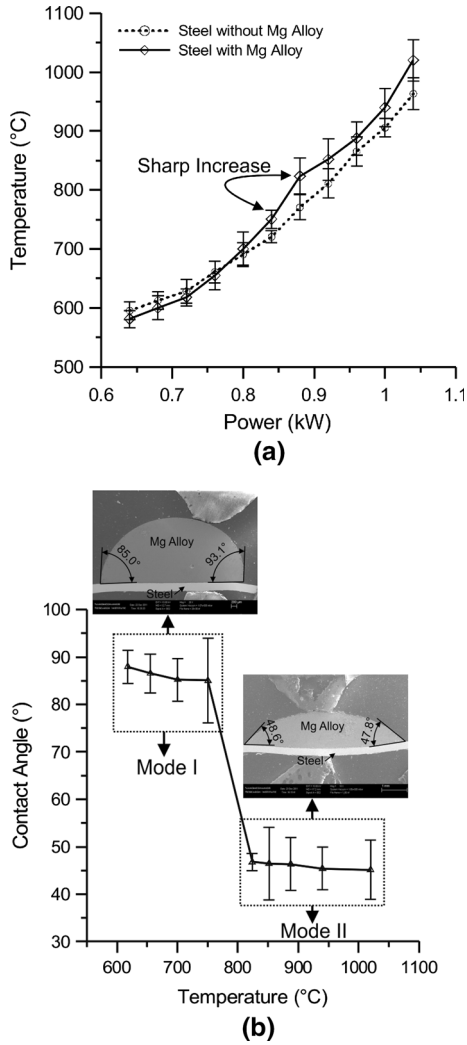


Fig. 2—(*a*) The peak temperature of the wetting tests *vs* laser beam power and (*b*) the contact angle as a function of the peak temperature during wetting experiments are shown.

### A. *Contact Angle vs Temperature*

Figure 2(a) shows the maximum measured temperature from the back side of the steel sheet *vs* the laser powers used in this study. As expected, increasing laser power resulted in increasing the maximum measured temperature. A linear behavior for temperature was

expected to be observed with increase of the laser power. However, a rapid increase of the temperature was found when the laser power was increased from 0.84 kW to 0.88 kW. To understand this behavior, the same experiments were carried out using Ni-plated steel without Mg alloy. The results are shown with a dashed line in Figure 2(a). Interestingly, a reasonable increase of temperature with increase of the laser power with almost a linear behavior was observed. Therefore, the cause of this rapid jump in the temperature-power profile could be related to possible exothermic reactions when Ni-plated steel and Mg alloy exist together. Further microstructural analyses, discussed in the subsequent sections, were performed to aid in studying this hypothesis.

Next the contact angles were measured from specimens produced with different laser parameters and hence different peak experiment temperatures. The contact angle as a function of peak temperature for the AZ92 Mg alloy on Ni-plated steel is shown in Figure 2(b). The contact angle of the alloy started from an initial value of about 88 deg at peak temperature of 891 K (618 °C). From this temperature, the contact angle remained almost constant for temperatures upto 1023 K (750 °C). This stage was denoted as the first wetting mode in this study (*i.e.*, Mode I). When the temperature was increased above 1023 K (750 °C), a sharp drop in the contact angle value was observed from around 85 to 47 deg and it again remained constant for increasing temperatures upto 1293 K (1020 °C). The wetting behavior in this temperature range was denoted as the second wetting mode (*i.e.*, Mode II). Cross-sectional views of the wetting samples at laser beam powers of 0.72 kW (in Mode I) and 0.92 kW (in Mode II) are presented in Figure 2(b). Peak temperatures above this level in the wetting experiments resulted in evaporation of magnesium as well as oxidation of liquid magnesium with excessive expulsion. Therefore, higher powers and temperatures were not explored further.

As a general result, a slight decrease of the contact angle with increasing temperature in each wetting mode was also observed (~2.9 and 1.6 deg for Modes I and II, respectively), indicating the effect of temperature on the improvement of the wetting.[2] The temperature driven change in contact angle, however, was not significant compared to the sharp drop of the contact angle from Mode I to Mode II (~38.3 deg).

To study possible formed reaction products along the Mg alloy-substrate interface in each wetting mode, microstructural analysis of the interfaces were performed as follows.

## B. *Interfacial Reaction Products*

### 1. *Mode I [891 K to 1023 K (618 °C to 750 °C)]*

Figures 3(a) through (d) shows the SEM micrographs of the Mg alloy-substrate interface of the wettability samples in the temperature range of 891 K to 1023 K (618 °C to 750 °C) (Mode I). In this mode, microstructural analysis of the interface (see Figures 3(a) through (d)) confirmed that an additional phase was formed along the Mg alloy-substrate interface. Figures 3(e) and (f) shows TEM image and the selected area diffraction patterns (SADP) of the interfacial phase, respectively. The diffraction pattern showed a standard pattern of AlNi (with BCC crystal structure) with [011] zone axis of the particle. According to the EDS analysis results, these faceted dendritic-shaped phases contained 49.6 ± 1.3 at. pct Ni, 45.4 ± 4.7 at. pct Al, and 5.0 ± 2.5 at. pct Mg, confirming that the phases identified in Figures 3(a) through (d) were mainly composed of AlNi intermetallic compound. It has been reported that each of the Al-Ni binary intermetallic compounds has some solubility for substitutional magnesium atoms.[17]

Continuous growth of the AlNi layer was found with increasing peak temperature. This phase formed as a result of a chemical reaction between Al from the molten Mg alloy and the Ni layer. When this AlNi phase formed, growth occurred *via* a diffusion mechanism at the interface from 0.5 $\mu$m thick at 891 K (618 °C) to 1.1 $\mu$m thick at 1023 K (750 °C). It is worth noting that the Ni layer still existed between the created AlNi layer and steel in this temperature range.

Figure 4 shows bright field TEM images of the Mg alloy-Ni interface in Mode I. The TEM analysis of the AlNi-Ni interface showed that the AlNi phase did not grow on the Ni, but instead nucleated and grew as a continuous layer adjacent to the interface. As shown in Figures 4(a) and (b), a continuous interlayer (100 to 400 nm thick) phase was observed along the interface between the AlNi phase and Ni. Higher magnification of this layer (shown in Figure 4(b)) confirmed good bonding between this layer and AlNi as well as to the Ni. To analyze the composition of the interfacial phase, scanning transmission electron microscopy (STEM)-EDS was used. The results showed that the interfacial layer contained an average of 65.8 ± 7.1 at. pct Mg and 34.2 ± 8.9 at. pct Ni.

To identify this Mg-Ni layer, SADP analysis of this layer was performed. Figures 4(c) and (d) show the SADP analysis of the Ni grain and Mg-Ni phase, respectively, when the incident beam was parallel to $[\bar{3}300]$ zone axis of the Mg-Ni phase. The interfacial phase in between AlNi phase and Ni-electrodeposited layer corresponded to $Mg_2Ni$ with Hexagonal Close-Packed (HCP) crystal structure. Therefore, in Mode I, AlNi + $Mg_2Ni$ reaction products were produced between Mg and steel (Mg-AlNi-$Mg_2Ni$-Ni-Fe). As a result, AlNi phase was identified as the immediate reaction product in contact with the Mg alloy.

### 2. *Mode II [1097 K to 1293 K (824 °C to 1020 °C)]*

Figure 5 shows the SEM photomicrographs of the Mg alloy-substrate interface for the temperature range of 1097 K to 1293 K (824 °C to 1020 °C) (Mode II). In this mode, the Ni coating was not detected as a separate layer along the interface after the wetting test and it was completely melted and dissolved into the Mg alloy (see Figure 5). As a result, a high volume fraction of AlNi was formed close to the interface in the molten area. The continuous growth of the AlNi was observed at the interface. Formation of diamond-shaped AlNi particles even far from the interface confirmed diffusion of Ni atoms into the Mg alloy (see Figure 5(h)). Therefore, the

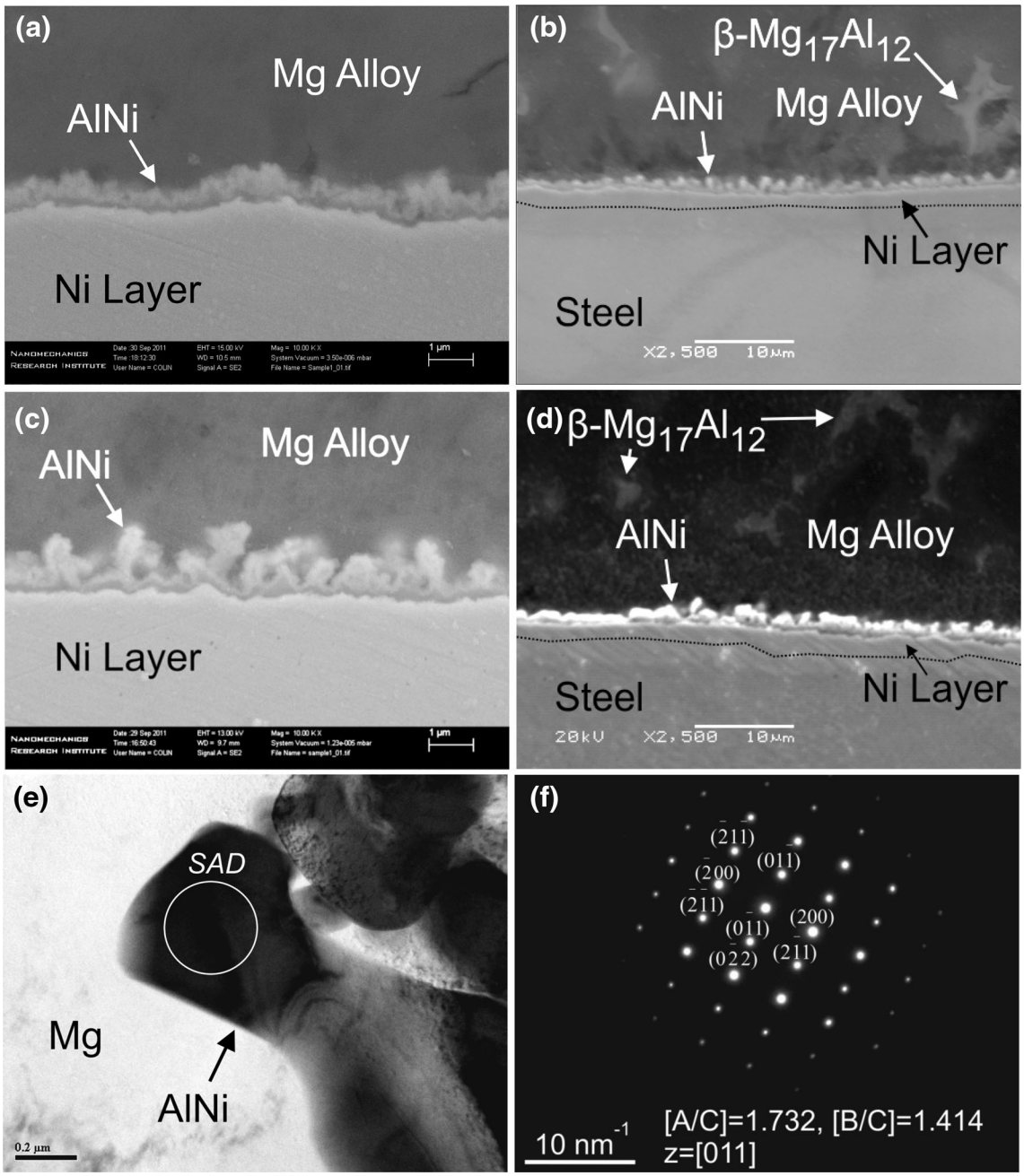


Fig. 3—The SEM micrographs of the Mg alloy-steel interface of the wetting sample at peak temperatures of (*a*) 891 K (618 °C), (*b*) 928 K (655 °C), (*c*) 973 K (700 °C), (*d*) 1023 K (750 °C), (*e*) TEM image of AlNi particle, and (*f*) SADP in the [011] zone axis of AlNi particle.

test duration and temperature were high enough for the entire Ni coating to melt and diffuse into the Mg alloy and as a result, AlNi particles crystallized even in the center of the molten region. For formation of AlNi, Al atoms from the Mg alloy react with the diffused Ni atoms from the interface. Therefore, AlNi particles are surrounded by Mg-Al alloy depleted in Al, shown as a dark gray phase around each AlNi particle.

Figure 6(a) shows a STEM image of the steel-Mg alloy interface from the specimen in Mode II. Growth of an intermediate phase was also found at the interface on the Fe grains. To identify the composition of formed phase(s) along the Mg alloy-steel interface, EDS mapping and line scan analysis were used, as shown in Figures 6(b) and (c), respectively. Representative concentration maps for Mg, Al, Ni, and Fe elements from the area shown in Figure 6(a) confirmed high concentration of Al and Ni at the interface. The distribution of elements across the interface (Figure 6(c)) showed that the interfacial phase contained $40.6 \pm 0.7$ at. pct Ni, $51.1 \pm 2.5$ at. pct Al, and $8.1 \pm 2.6$ at. pct Fe, confirming that the interfacial phase in Figure 6(a) was mainly composed of AlNi intermetallic compound. The results also showed a slight interdiffusion of Ni and Al to the Fe grains as a result of high temperature experienced during the wetting exper-

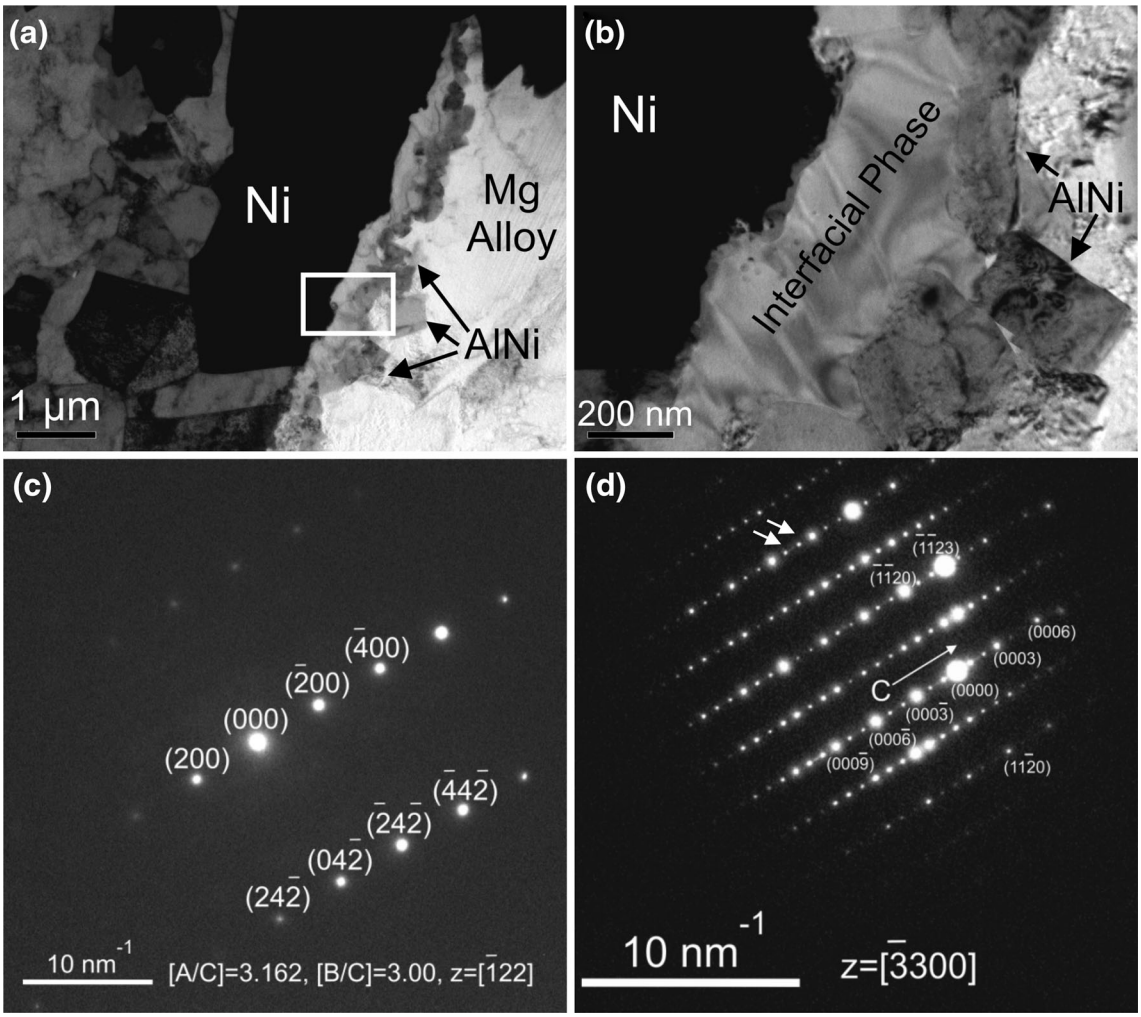


Fig. 4—(*a*) and (*b*) TEM images of the Mg alloy-Ni-coated steel interface at different magnifications, (*c*) the SADP of the Ni grain substrate, when incident beam was parallel to $[\bar{1}22]_{Ni}$ and (*d*) the corresponding SADP of the formed Mg-Ni phase at the interface, when the incident beam was parallel to $[\bar{3}300]_{Mg-Ni}$.

iment. The SADP analysis also identified the phase as AlNi grains. Therefore, in Mode II, AlNi was the only reaction product between Mg and steel (Mg-AlNi-Fe).

As discussed in Section II–A, a sharp increase of the temperature was observed in Figure 2(a) when the laser power was increased from 0.84 kW (with slight formation of AlNi) to 0.88 kW (with heavily nucleation of AlNi). Gasparyan and Shteinberg[18] used a specially designed differential thermal analysis to show that reactions between Al and Ni are highly exothermic. The heat provided during these wetting tests by laser can initiate exothermic reactions. Therefore, the exothermic nature of the Al-Ni interaction was the mechanism behind the sharp increase of the peak temperature when the laser power was high enough to initiate this reaction. The released heat is dependent on the volume fraction of the precipitated AlNi phase, which significantly increased when the laser power increased from 0.84 to 0.88 kW (compare Figures 3 and 5). Additionally, the partial enthalpies of mixing of Al-Ni reactions are high.[18] These phenomena generate high local temperatures near the steel-Mg alloy interface leading to the sharp increase of the peak temperature recorded in Figure 2(a).

The formed reaction products in the temperature range of 891 K to 1293 K (618 °C to 1020 °C) are in agreement with the predicted phase stability map obtained by Nasiri *et al.*[3] They used a computational thermodynamic analysis in non-equilibrium conditions in order to predict the phases most likely to form along the interface between Ni-electroplated steel and AZ92 Mg alloy at different temperatures and compositions.[3] As a result, AlNi + $Mg_2Ni$ and AlNi were predicted to form along the Mg alloy-steel interface in the temperature range of 873 K to 1023 K (600 °C to 750 °C) and 1023 K to 1373 K (750 °C to 1100 °C), respectively[3].

In this study, different contact angles at temperatures higher than 891 K (618 °C) were associated with the formation of different reaction products between Mg alloy and steel. In Mode I [891 K (618 °C) ≤ $T_{max}$ ≤ 1023 K (750 °C)], the Ni-plated steel was covered by a continuous layer of $Mg_2Ni$, which extended across the

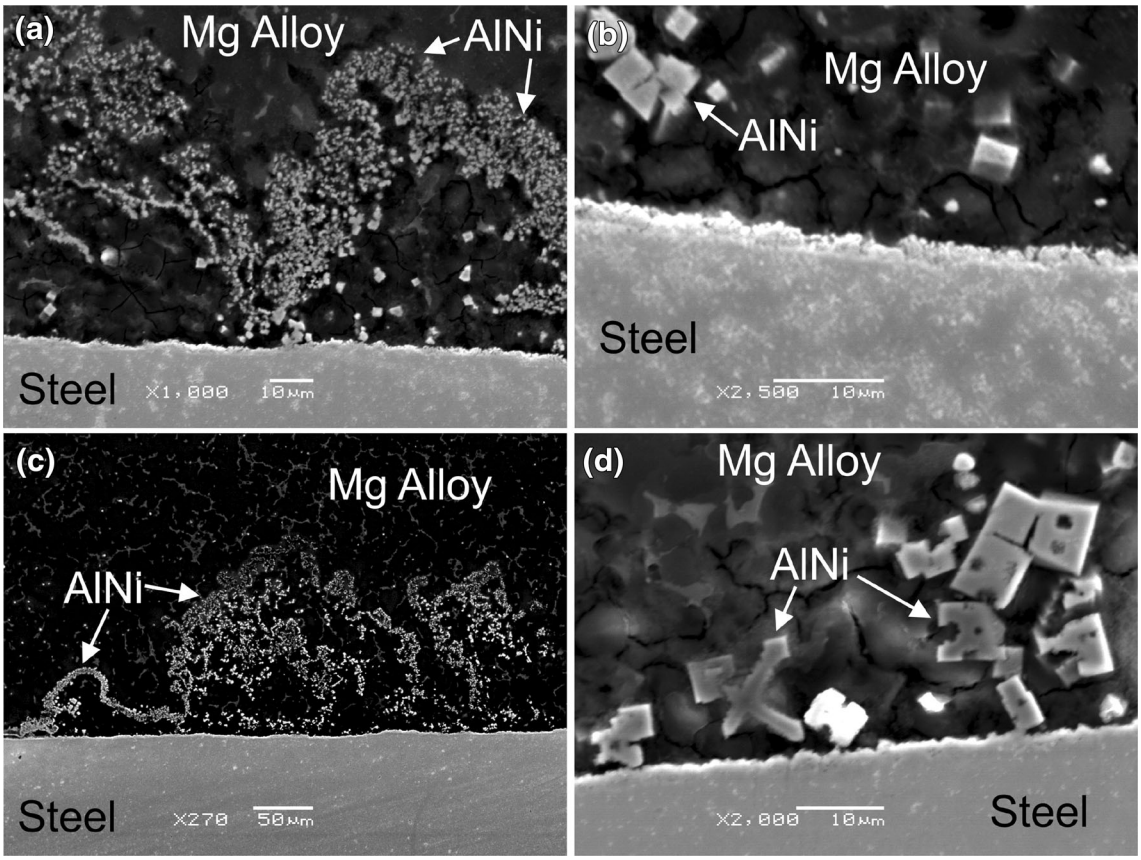


Fig. 5—The SEM micrographs of the Mg alloy-steel interface of the wetting samples at peak temperatures of (*a*) and (*b*) 1097 K (824 °C), (*c*) and (*d*) 1125 K (852 °C), (*e*) and (*f*) 1161 K (888 °C), (*g*) and (*h*) 1213 K (940 °C).

solid-liquid interface. However, the AlNi layer on top of $Mg_2Ni$ was the phase in contact with remaining liquid (Mg alloy). In comparison, in Mode II [1097 K (824 °C) ≤ $T_{max}$ ≤ 1293 K (1020 °C)], the steel (Fe grains) was covered by a continuous layer of the AlNi compound. Therefore, in both Modes I and II the reaction product in contact with Mg alloy was AlNi phase, but the contact angle differed greatly in these two cases. Similar to the spreading behavior observed by Saiz *et al.*,[7] this phenomenon cannot be explained using previously proposed wetting mechanisms for metallic-metallic reactive systems. In the following section, the mechanism behind the two different wetting modes will be investigated, which will identify some major factors affecting the reactive wetting in a metallic-metallic system.

### C. *Lattice Mismatching between Reaction Products and Substrates*

#### 1. *Mode I (Mg-AlNi-$Mg_2Ni$-Ni-Fe)*

For both Modes I and II, AlNi is the first precipitated phase from the liquid. Therefore, after formation of this phase along the interface, the remaining liquid will be in direct contact with AlNi and this phase plays the role of substrate for the remaining liquid. As a result, the Mg-AlNi interface will form after solidification of the liquid Mg in both wetting modes, meaning the energy of this interface cannot be the driving force for the wetting nor explain the observed difference in the wetting behavior in this system. However, the lattice matching and crystal orientations at the Mg-AlNi interface were studied using a series of SADP analyses as well as HR-TEM examinations, shown in Figure 7. The SADP of the AlNi phase was taken in the direction along the zone axis of $[011]_{AlNi}$. The diffraction pattern of the Mg phase with a ring pattern showed that the *d*-value of the $\{20\bar{2}0\}_{Mg}$ and $\{11\bar{2}2\}_{Mg}$ planes are the same as that of $(200)_{AlNi}$ and $(02\bar{2})_{AlNi}$, respectively (see Figure 7(c)). Figure 7(d) shows the HR-TEM image of Mg-AlNi interface. When $[001]_{AlNi}//[01\bar{1}1]_{Mg}$, the orientation relationship (OR) of AlNi phase and Mg was found to be $\{10\bar{1}1\}_{Mg}$ 113.1 deg from $\{110\}_{AlNi}$ (see Figure 7(d)). The measured interplanar spacings were 2.423 Å and 2.070 Å for $\{10\bar{1}1\}_{Mg}$ and $\{110\}_{AlNi}$, respectively, which provides 17 pct interplanar mismatch at the interface.

Moving from the Mg-AlNi interface to the substrate direction, the next formed interface was the AlNi-$Mg_2Ni$ interface. SADP analysis of this interface did not show any overlapping diffraction spots, meaning no specific OR was found between these two phases at their interface. Figure 8 shows the HR-TEM image of the AlNi-$Mg_2Ni$ interface, when $[001]_{AlNi}//[0001]_{Mg_2Ni}$. The crystallographic orientation between the AlNi and $Mg_2Ni$ phases in this site was determined to be $\{110\}_{AlNi}$ 25.0 deg from $\{10\bar{1}0\}_{Mg_2Ni}$ and the measured interplanar spacing for these planes were $d_{\{110\}AlNi}$ = 2.10 Å and $d_{\{10\bar{1}0\}Mg_2Ni}$ = 4.290 Å, which provides

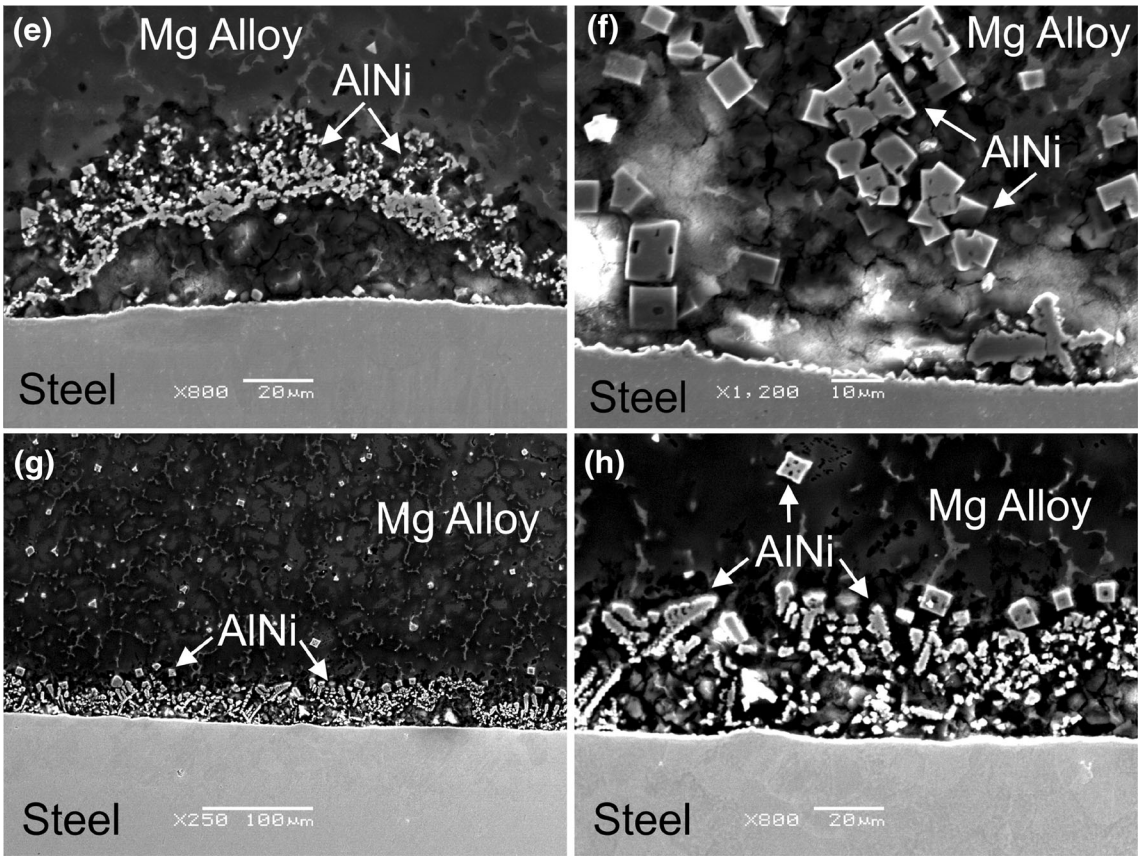


Fig. 5—continued.

104.3 pct interplanar mismatch at the interface. Therefore, the HR-TEM results did not show an OR with low mismatch strain in the AlNi-$Mg_2Ni$ adjoining lattices.

In Mode I, $Mg_2Ni$ is also in contact with the Ni layer from the other side. The SADP analysis of the $Mg_2Ni$-Ni interface (shown in Figures 4 and 9) confirmed that the lattice of the Ni was exactly located on the $[\bar{1}22]$ zone axis, when the $Mg_2Ni$ phase was parallel to the $[\bar{3}300]$ zone axis. This result implies that the OR between the Ni grain and formed $Mg_2Ni$ phase at the interface was $[\bar{3}300]_{Mg_2Ni}//[\bar{1}22]_{Ni}$. However, none of the $Mg_2Ni$ diffraction spots were superimposed with Ni diffraction spots (see Figure 9(b)), meaning that none of the diffracted planes in Figure 9(b) were parallel to each other, when the electron beam was parallel to the $[\bar{1}22]$ zone axis of the Ni.

Figure 9(c) shows the HR-TEM image of the $Mg_2Ni$-Ni interface showing the matching planes and crystal orientation between $Mg_2Ni$ and Ni, when $[01\bar{1}0]_{Mg_2Ni}//[1\bar{1}0]_{Ni}$. According to this HR analysis, with reference to HCP crystal structure for the $Mg_2Ni$ phase, the *d*-spacing of the parallel planes of the $Mg_2Ni$ phase shown in Figure 9(c) was measured to be 1.324 nm, which is close to the published *c*-value of $Mg_2Ni$ phase (at 44.2 at. pct Ni, $a_{Mg_2Ni} = 0.518$ nm, $c_{Mg_2Ni} = 1.319$ nm[19]). Therefore, the parallel planes of $Mg_2Ni$ phase in Figure 9(c) correspond to (0001) planes (basal planes in HCP). However, the SADP of this phase shows the extra reflection spots at positions of n/3 $(0003)_{HCP}$ (n is an integer), as marked with the arrow heads in Figure 4(d). This diffraction pattern of the interfacial phase shows a long-period ordered structure.[20] This phase has basically an ordered hexagonal crystal lattice, but the stacking order of the close-packed planes is modulated in the [0001] or [0003] direction at every third layer and the stacking sequence can thus be described as ABB (see Figure 10). Due to ABBABB… modulation, the original reciprocal lattice points are split into three in the direction of the modulation, [0003]. A characteristic of the split spots is that they always lie on the same levels in the direction of the [0001] axis of stacking and divide the distance between the origin and (0003) spot into three segments. An arrangement of bright dots in the HR-TEM image of Figure 10(a) clearly indicates the stacking sequence of ABBABB… with a period of 1.324 nm. Therefore, when considering the ordering of the atoms, the distribution of the superlattice spots in the $Mg_2Ni$ interfacial phase did not agree with the distribution of the normal HCP lattice spots (see Figure 10(b)). Considering the distortion from the 2H-type (ABAB…) period ordered structure, the present long-period ordered structure of the $Mg_2Ni$ phase can be described by a hexagonal lattice with $a_H = 0.518$ nm and $c_H = 1.324$ nm, as shown in Figure 10(b) and the reflections have been indexed accordingly.

The HR-TEM image (Figure 9(c)) indicated that the crystallographic OR between the reaction product ($Mg_2Ni$ phase) and the substrate (Ni layer) in this site was determined to be $\{0003\}_{Mg_2Ni}$ 56.6 deg from $\{111\}_{Ni}$ and the measured interplanar spacing for these

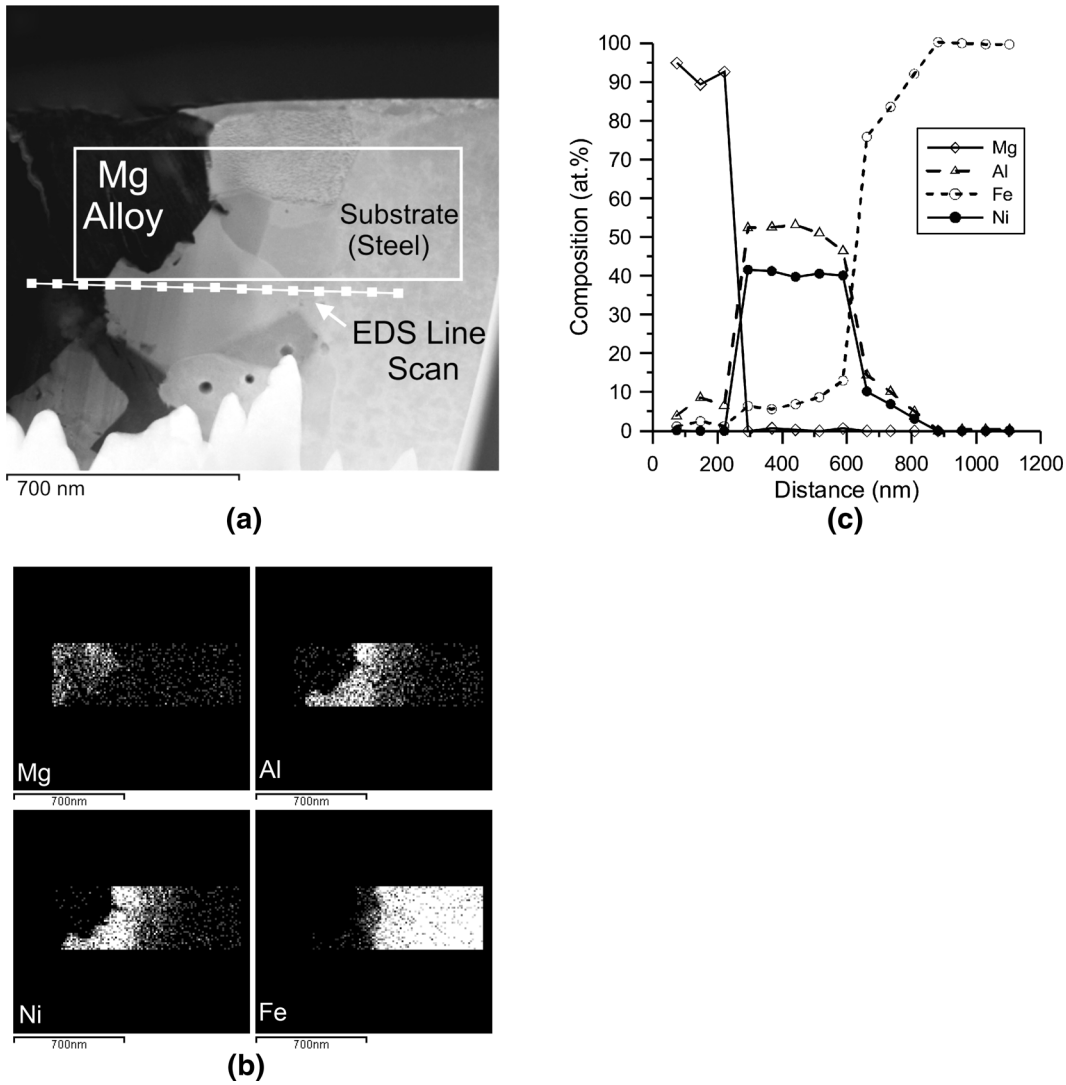


Fig. 6—(*a*) STEM image of Mg alloy-steel interface showing grains of the interfacial phase, (*b*) representative concentration maps of Mg, Al, Ni, and Fe elements across the interface, and (*c*) STEM-EDS point analysis results across the shown line in a.

planes were $d_{\{0003\}Mg_2Ni} = 4.415$ Å and $d_{\{111\}Ni} = 2.060$ Å, which provides 114 pct interplanar mismatch at the interface. Therefore, the SADP analysis and also HR-TEM results did not show an OR with low mismatch strain in the $Mg_2Ni$-Ni adjoining lattices.

Due to extensive solid solubility of Ni and Fe into each other (a continuous solid solution with unlimited solubility is formed between Ni and Fe at high temperature[19]), thus defining a distinct interface between the Ni layer and Fe, where their adjoining lattices meet, was not possible. This solubility minimizes the mismatch strain between Ni and Fe.

### D. *Mode II (Mg-AlNi-Fe)*

Figure 11 shows a HR-TEM image of the Mg-AlNi interface in Mode II. In this mode, an OR similar to that between Mg and AlNi in Mode I was found [when $[001]_{AlNi}//[01\bar{1}1]_{Mg}$, $\{10\bar{1}1\}_{Mg}$ 95.3 deg from $\{110\}_{AlNi}$ (see Figure 11)]. The measured interplanar spacings were 2.402 and 2.041 Å for $\{10\bar{1}1\}_{Mg}$ and $\{110\}_{AlNi}$, respectively, which provides 18 pct interplanar mismatch at the interface.

To analyze AlNi-Fe interface, the SADP and HR-TEM analysis of this interface were also performed. Figure 12 shows a TEM image of one AlNi grain formed as the reaction product at the interface surrounded by Fe grains from the substrate. In this area, both AlNi and Fe were single crystals (one grain). In order to identify the OR between the AlNi phase and the Fe grain, first the TEM foil was tilted until the incident beam was parallel to the [011] zone axis of the Fe grain, as shown in Figure 12(a) and the SADP shown in Figure 12(b) was taken from the Fe grain. Then without changing the orientation of the beam and specimen with respect to each other, the SADP of the AlNi grain and also the AlNi-Fe interface were taken, as shown in Figures 12(c) and (d), respectively. These results showed that the grain of the AlNi phase was exactly located on $[011]_{AlNi}$ zone axis, when Fe was parallel to $[011]_{Fe}$ zone axis. These results imply that the OR between formed AlNi interfacial phase and Fe grain (both having BCC

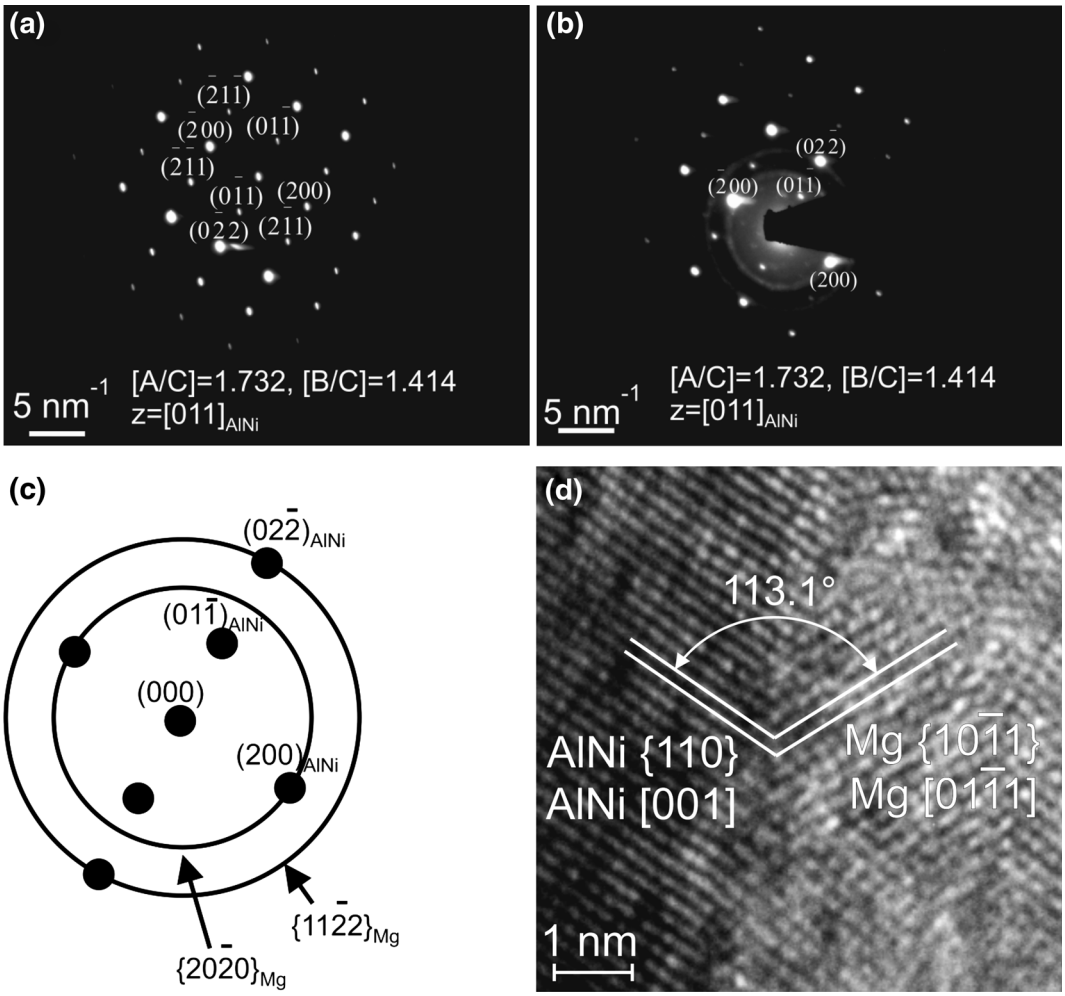


Fig. 7—(*a*) The SADP of the AlNi grain, when incident beam was parallel to $[011]_{AlNi}$, (*b*) the corresponding SADP of the Mg-AlNi interface, (*c*) the schematic representing OR between Mg and AlNi grain at the interface, and (*d*) HR-TEM image of Mg-AlNi interface.

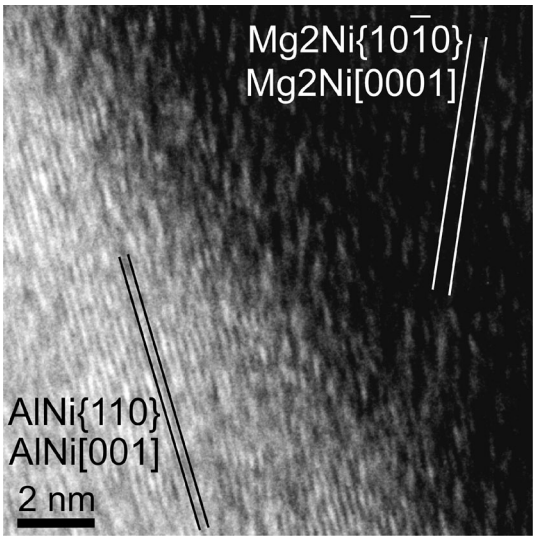


Fig. 8—HR-TEM image of the AlNi-$Mg_2Ni$ interface.

crystal structure) at their interface was $[0\bar{1}1]_{AlNi}//[011]_{Fe}$. Furthermore, the diffraction spot of $(\bar{2}11)_{Fe}$ was superimposed with that of $(\bar{2}00)_{AlNi}$, as shown in Figures 12(d) and (e). This indicates that the crystallographic plane relationship between the formed AlNi grain at the interface and Fe grain in this site was $(\bar{2}00)_{AlNi}//(\bar{2}11)_{Fe}$.

Figure 13 shows the HR-TEM image of the AlNi-Fe interface. The boundary between these two phases was very smooth and difficult to distinguish due to good lattice plane matching between Fe and AlNi at the interface. This HR-TEM image also indicates that the crystallographic OR between the formed AlNi grain (reaction product) and Fe grain (substrate) at the interface in this site is $\{110\}_{AlNi}$ 99 deg from $\{110\}_{Fe}$, when $[001]_{AlNi}//[001]_{Fe}$.

The HR-TEM image indicated that the measured interplanar spacing for these planes were $d_{\{110\}Fe}$ = 2.151 Å and $d_{\{110\}AlNi}$ = 2.046 Å, which provides 5 pct interplanar mismatch at the interface. Therefore, the SADP analysis and also HR-TEM results confirmed a low interfacial mismatch strain between AlNi phase and Fe.

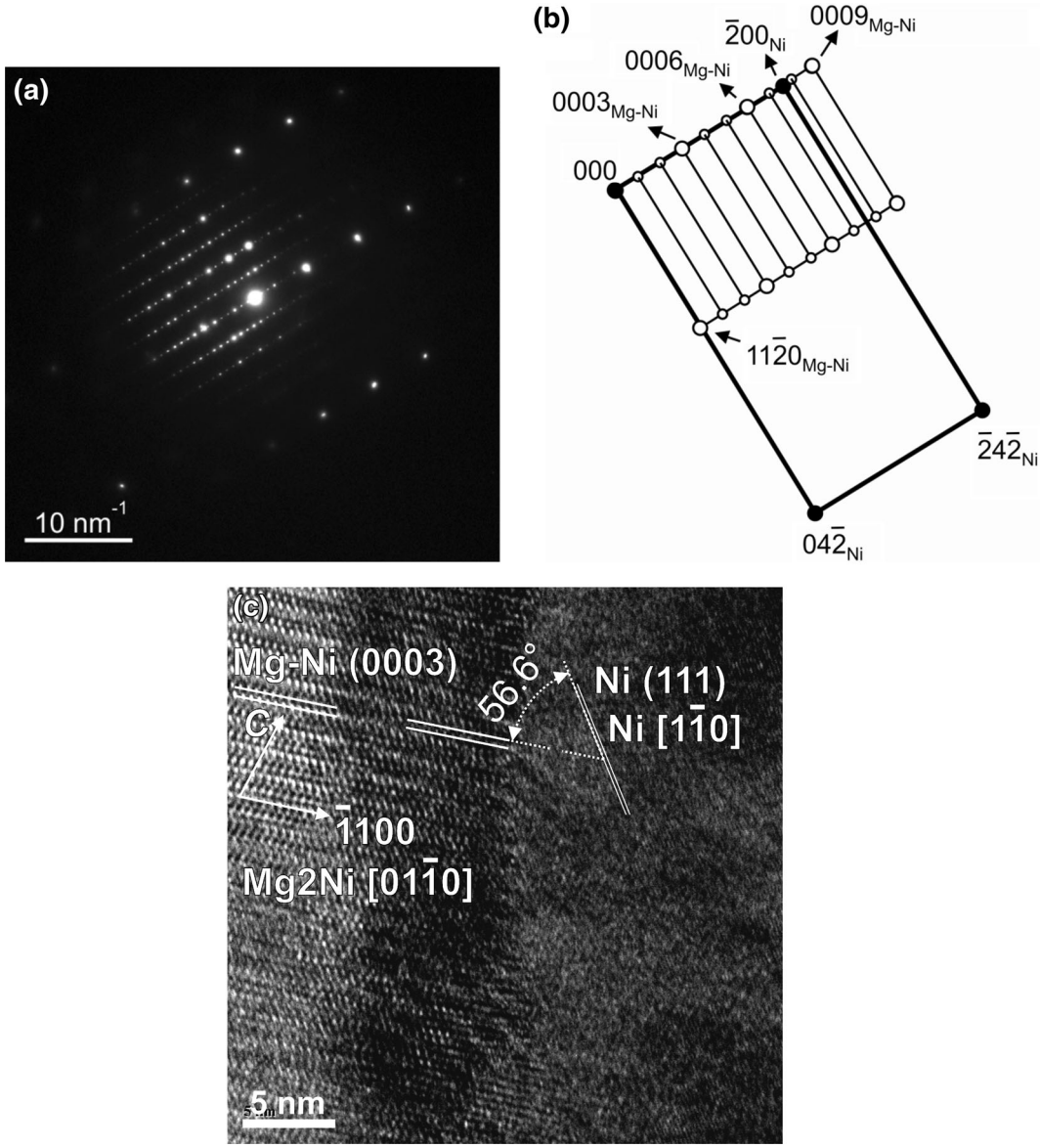


Fig. 9—(*a*) SADP of the $Mg_2Ni$-Ni interface, (*b*) the schematic representing OR between $Mg_2Ni$ phase and Ni grain at the interface ($[\bar{3}300]_{Mg_2Ni}//[\bar{1}22]_{Ni}$), and (*c*) HR-TEM image of $Mg_2Ni$-Ni interface showing the matching planes and crystal orientation at the interface.

### E. *Theoretical Calculation Results*

The HR-TEM measurements indicated ORs and lattice matching between each of the observed interfaces in this study. However, the observed ORs were more like a local observation at the interface than a general trend of OR. Therefore, further analysis of the possible formed ORs at the interface is required. Due to different lattice parameters between Mg, AlNi, $Mg_2Ni$, Ni, and Fe, an intrinsic strain in their adjoining lattices arises. If this strain is not relaxed by the introduction of misfit dislocations, the magnitude of this extensional strain will be proportional to the lattice mismatch between each two phases at the interface.[8] This strain will increase the total interfacial energy. In such a way, the interfacial energy and, therefore, the wetting can be dependent on the crystallographic dis-registry and lattice matching along *AlNi-$Mg_2$Ni-Ni* and *AlNi-Fe* adjoining lattices, in modes I and II, respectively. In addition, the effectiveness of a substrate in promoting heterogeneous nucleation, such as Ni for $Mg_2Ni$ or Fe for AlNi, depends on the crystallographic OR and lattice matching between the substrate and the solidified region.[21]

For each of the observed interfaces in this study, one interface, which is the intersection plane of the matching planes, forms in between the phase and the substrate. This plane consists of a series of matched atom rows. In order to minimize the strain energy at the interface, the interatomic spacing misfit along the matching direction should be minimized.[22] The strain energy at the interface is also affected by the interplanar spacing (*d*-value) mismatch between the matching planes.[22] During phase formation (*e.g.*, formation of $Mg_2Ni$ between Ni and AlNi, or AlNi on Fe), to minimize the

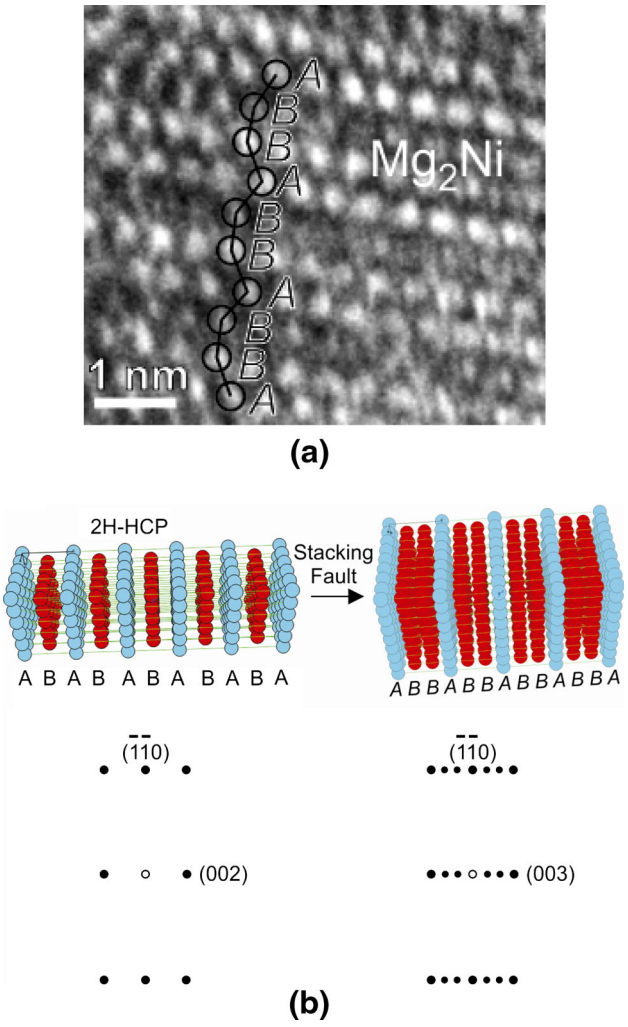


Fig. 10—(*a*) HR-TEM image of $Mg_2Ni$ phase and (*b*) schematic illustration showing a structural relationship between the HCP-$Mg_2Ni$ (2H-type) and long-period ordered $Mg_2Ni$ observed in this study, together with the corresponding computed SADPs. The $Mg_2Ni$ atomic structure model was constructed using $Mg_2Ni$ lattice parameters ($a_{HCP}$ = 0.518 nm and $c_{HCP}$ = 1.324 nm).

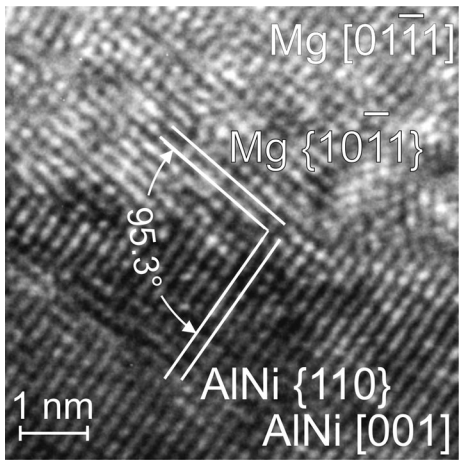


Fig. 11—HR-TEM image of the Mg-AlNi interface in Mode II.

free energy of the system, the system tries to find matching planes with small *d*-value mismatch.

To further study possible formed ORs along Mg-AlNi-$Mg_2Ni$-Ni and Mg-AlNi-Fe interfaces, the edge-to-edge crystallographic model was used.[22,23] This model was developed by Zhang and Kelly[22,23] from the lattice matching model. In this matching model, the matching directions and matching planes are the close or nearly close-packed directions and planes.[22,23] The interatomic misfit and interplanar mismatch between two phases can be calculated by

$$\delta = \frac{|\Delta a_0|}{a_0} \qquad [2]$$

where $\Delta a_0$ is difference between interatomic or interplanar spacing of the two phases and $a_0$ is the interatomic or interplanar spacing of the substrate for a specific direction or plane.[22] The calculation procedure and the results of the interatomic spacing misfits along matching directions and interplanar spacing mismatches between matching planes for different formed interfaces in this study are given in the Appendix.

In Mode I, the calculated minimum interplanar mismatch was 16.4 pct ($\{10\bar{1}1\}_{Mg}//\{110\}_{AlNi}$)-108.3 pct ($\{110\}_{AlNi}//\{10\bar{1}1\}_{Mg_2Ni}$)-17.2 pct ($\{10\bar{1}1\}_{Mg_2Ni}//\{100\}_{Ni}$). These results showed that no possible pair of planes between $Mg_2Ni$ phase and Ni from one side and AlNi from the other side was found to form an OR with low mismatch strain in their adjoining lattices. These predicted results are in agreement with the observed interplanar mismatch for different formed interfaces in Mode I, as shown in Figures 7, 8, 9, and 10 (17 pct ($\{10\bar{1}1\}_{Mg}//\{110\}_{AlNi}$)-104.3 pct ($\{110\}_{AlNi}//\{10\bar{1}0\}_{Mg_2Ni}$)-114 pct ($\{0003\}_{Mg_2Ni}//\{111\}_{Ni}$)). Therefore, the formed $Mg_2Ni$ phase, tolerates high interfacial mismatch strain energy from its both sides. This causes poor wetting of Ni by Mg when $Mg_2Ni$ phase forms as the reaction product between AlNi and Ni. The results of the AlNi (BCC)-Mg (HCP) interface also showed that there was no potential matching planes between Mg and AlNi with low mismatch strain.

In Mode II, the calculated minimum interplanar mismatch was 16.4 pct ($\{10\bar{1}1\}_{Mg}//\{110\}_{AlNi}$)-0.6 pct ($\{111\}_{AlNi}//\{111\}_{Fe}$). This leads to a low mismatch strain between AlNi and Fe and a low interfacial energy and promoted the wetting of Fe substrate by Mg when AlNi phase forms as the reaction product on the substrate. The presented experimental results in Figures 11 and 13 also confirmed low mismatch strain between Fe substrate and AlNi phase at the interface (18 pct ($\{10\bar{1}1\}_{Mg}//\{110\}_{AlNi}$)-5 pct ($\{110\}_{AlNi}//\{110\}_{Fe}$)).

Table III summarizes the wetting behavior of the Ni-electroplated steel by molten Mg alloy at different wetting modes analyzed in the current study. Presented results in this study for a strong interaction metallic-metallic system proved that the wetting behavior can be very much affected by the reaction products, which are not even in direct contact with the liquid phase; $Mg_2Ni$ in this study. More specifically, the lattice mismatching between different reaction products, and the reaction product and the substrate play a major role in reactive wetting. Lattice mismatch between reaction products

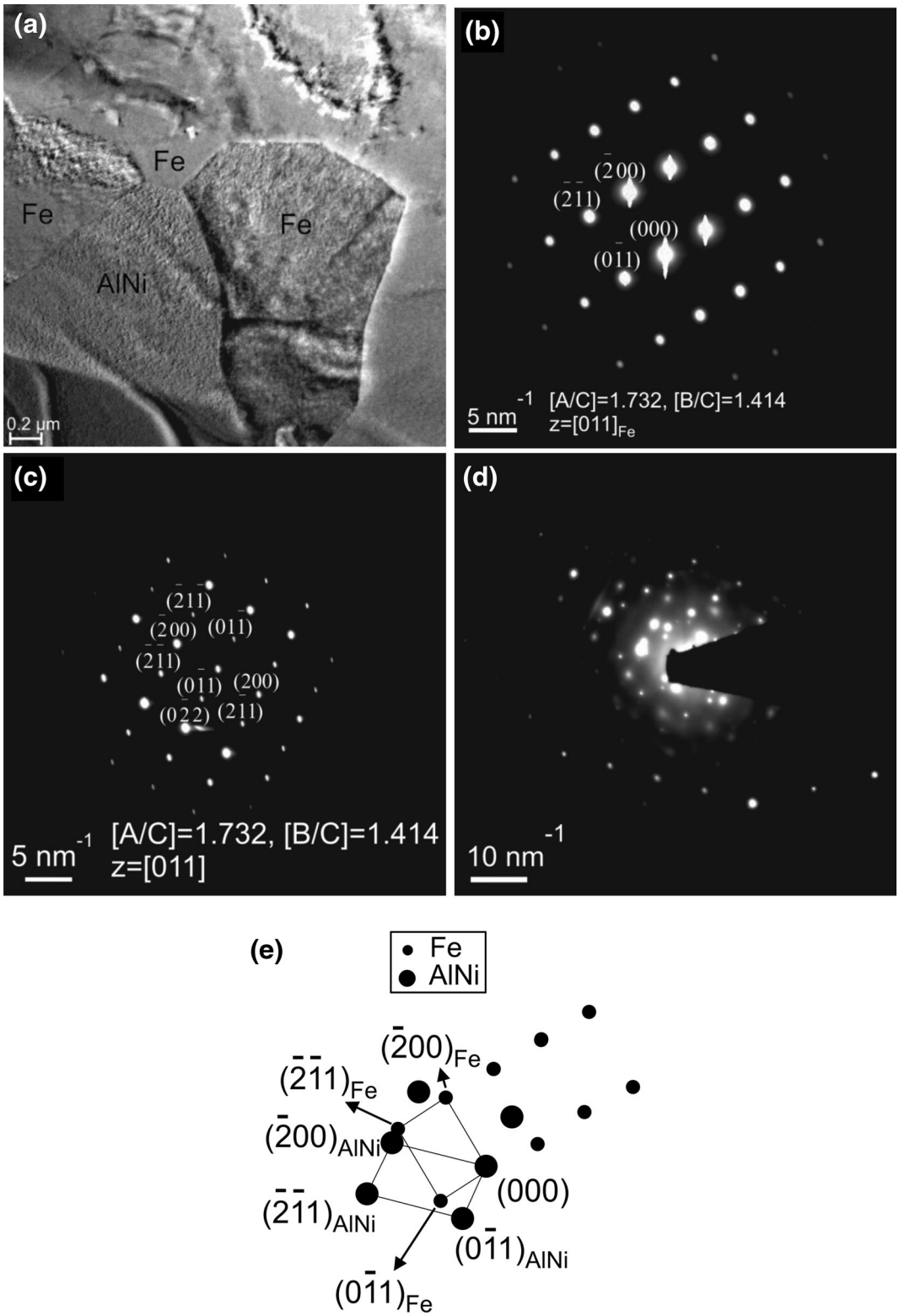


Fig. 12—(*a*) TEM image of the AlNi and Fe grains at the interface of Mg alloy-steel, (*b*) SADP of Fe grain, (*c*) the corresponding SADP of AlNi grain, (*d*) SADP of the AlNi-Fe interface (incident beam was parallel to $[011]_{AlNi}//[011]_{Fe}$), and (*e*) the schematic showing the OR between AlNi and Fe grains at the interface.

themselves or a reaction product and a substrate might prevent the wetting of the substrate by the liquid.

The results of this work confirmed the relationship between interfacial phases and wetting characteristics in the Ni-plated steel-AZ92 Mg alloy couple with a metallurgical bond between the steel and Mg alloy. This will facilitate increased application and use of Mg alloys in the automotive and aerospace industries, where

Table III. Wetting Behavior of Ni-Plated Steel by Mg Alloy at Different Wetting Modes

| Temperature Range [K (°C)] | 891 K to 1023 K (618 °C to 750 °C) (Mode I) | 1097 K to 1293 K (824 °C to 1020 °C) (Mode II) |
|---|---|---|
| Contact Angle (deg) | 86 | 46 |
| Mg-Reaction Product(s)-Substrate | Mg-AlNi-$Mg_2Ni$-Ni-Fe | Mg-AlNi-Fe |
| Interplanar Mismatch from HR-TEM | 17 pct $(\{10\bar{1}1\}_{Mg}//\{110\}_{AlNi})$-104.3 pct $(\{110\}_{AlNi}//\{10\bar{1}0\}_{Mg_2Ni})$-114 pct $(\{0003\}_{Mg_2Ni}//\{111\}_{Ni})$ | 18 pct $(\{10\bar{1}1\}_{Mg}//\{110\}_{AlNi})$-5 pct $(\{110\}_{AlNi}//\{110\}_{Fe})$ |
| Minimum Interplanar Mismatch from Edge-to-Edge Model | 16.4 pct $(\{10\bar{1}1\}_{Mg}//\{110\}_{AlNi})$-108.3 pct $(\{110\}_{AlNi}//\{10\bar{1}\ 1\}_{Mg_2Ni})$-17.2 pct $(\{10\bar{1}1\}_{Mg_2Ni}//\{100\}_{Ni})$ | 16.4 pct $(\{10\bar{1}1\}_{Mg}//\{110\}_{AlNi})$-0.6 pct $(\{111\}_{AlNi}//\{111\}_{Fe})$ |

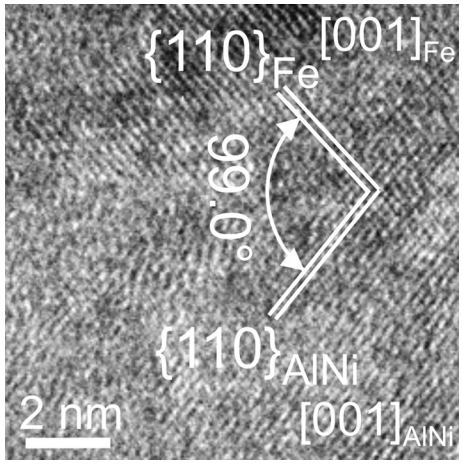


Fig. 13—HR-TEM image of the AlNi-Fe interface.

joining Mg alloys to steel in order to achieve light weight, versatile, and tailored properties in one composite part is highly desirable.

## III. CONCLUSIONS

Reactions between molten Mg alloy and Ni-electroplated steel led to the reduction of contact angle from 86 deg in the temperature range of 891 K to 1023 K (618 °C to 750 °C) (Mode I) to only 46 deg in the temperature range of 1097 K to 1293 K (824 °C to 1020 °C) (Mode II). In Mode I, formation of AlNi and $Mg_2Ni$ reaction products along the Mg-Ni interface with the measured interplanar mismatches of 17 pct $(\{10\bar{1}1\}_{Mg}//\{110\}_{AlNi})$-104.3 pct $(\{110\}_{AlNi}//\{10\bar{1}0\}_{Mg_2Ni})$-114 pct $(\{0003\}_{Mg_2Ni}//\{111\}_{Ni})$ were observed. In comparison, in Mode II, AlNi was the only formed reaction product along the Mg-Fe interface with the measured interplanar mismatches of 18 pct $(\{10\bar{1}1\}_{Mg}//\{110\}_{AlNi})$-5 pct $(\{110\}_{AlNi}//\{110\}_{Fe})$. Also, the calculated minimum interplanar mismatches using the edge-to-edge matching model were 16.4 pct $(\{10\bar{1}1\}_{Mg}//\{110\}_{AlNi})$-108.3 pct $(\{110\}_{AlNi}//\{10\bar{1}1\}_{Mg_2Ni})$-17.2 pct $(\{10\bar{1}1\}_{Mg_2Ni}//\{100\}_{Ni})$ for Mode I and 16.4 pct $(\{10\bar{1}1\}_{Mg}//\{110\}_{AlNi})$-0.6 pct $(\{111\}_{AlNi}//\{111\}_{Fe})$ for Mode II. Therefore, the results presented in this study confirmed that formation of $Mg_2Ni$ reaction product between AlNi and Ni substrate produced a large lattice mismatch between interfaces which results in an increase in the interfacial strain energy of the system and, therefore, wetting contact angle. It follows from this finding that the lattice mismatching at the interfaces between reaction product(s) and substrate, which are not in direct contact with liquid phase, can greatly influence the wetting of the liquid.

## ACKNOWLEDGMENTS

The authors wish to acknowledge support of the Magnesium Network of Canada (MagNET) supported by the Natural Sciences and Engineering Research Council of Canada (NSERC) and American Welding Society (AWS) Graduate Fellowship program for sponsoring this work.

## APPENDIX: LATTICE MATCHING CALCULATION USING EDGE-TO-EDGE MODEL

Table AI shows the close-packed directions and planes together with their interatomic or interplanar spacings as a function of lattice parameters for different crystal structures observed in this study.

### *Mg (HCP)-AlNi (BCC) Interface (Modes I & II)*

For the HCP and BCC crystal structures, there are three and four possible close-packed or nearly close-packed directions (directions with low indices), respectively (see Table AI). Among these directions, $\langle 10\bar{1}0\rangle_{HCP}$, $\langle 11\bar{2}3\rangle_{HCP}$, and $\langle 113\rangle_{BCC}$ are zigzag atom rows and the rest are straight atom rows.[22] Therefore, there are a total of five possible matching direction pairs between HCP and BCC. Table AII shows the calculated interatomic spacings for Mg and AlNi and interatomic misfits along possible matching directions between them. The lattice parameters used in the current study are $a_H$ = 0.320 nm and $c_H$ = 0.520 nm for Mg and $a_B$ = 0.288 nm for AlNi.[19] The calculated results (Table AII) indicate that if 10 pct is selected as the critical value of the interatomic spacing misfit, just direction pair of $\langle 11\bar{2}0\rangle_{Mg}//\langle 100\rangle_{AlNi}$ satisfies this condition. The selection of 10 pct as the critical value for the interatomic spacing misfit is based on van der

**Table AI. The Most Close-Packed Directions and Planes and their Interatomic and Interplanar Spacings for HCP, FCC, and BCC Crystal Structures**

| Crystal Structure | Close-Packed Direction | Interatomic Spacing | Close-Packed Plane | Interplanar Spacing |
|---|---|---|---|---|
| HCP ($a_H$, $c_H$)* | $\langle 11\bar{2}0\rangle$ | $a_H$ | {0002} | $c_H/2$ |
| | $\langle 10\bar{1}0\rangle$ | $0.5a_H\sqrt{3}$ | $\{10\bar{1}1\}$ | $\frac{a_H c_H \sqrt{3}}{\sqrt{4c_H^2+3a_H^2}}$ |
| | $\langle 11\bar{2}3\rangle$ | $0.5\left(a_H^2+c_H^2\right)^{0.5}$ | $\{10\bar{1}0\}$ | $\sqrt{3}a_H/2$ |
| FCC ($a_F$)* | $\langle 110\rangle$ | $\sqrt{2}/2 a_F$ | {111} | $\sqrt{3}/3 a_F$ |
| | $\langle 100\rangle$ | $a_F$ | {110} | $\sqrt{2}/2 a_F$ |
| | $\langle 111\rangle$ | $\sqrt{3}a_F$ | {100} | $a_F$ |
| BCC ($a_B$)* | $\langle 111\rangle$ | $\sqrt{3}/2 a_B$ | {110} | $\sqrt{2}/2 a_B$ |
| | $\langle 100\rangle$ | $a_B$ | {200} | $0.5a_B$ |
| | $\langle 110\rangle$ | $\sqrt{2}a_B$ | {111} | $\sqrt{3}/3 a_B$ |
| | $\langle 113\rangle$ | $0.25\sqrt{11}a_B$ | | |

*Lattice parameters.

**Table AII. Interatomic Spacing Misfits Along Possible Matching Directions Between Mg and AlNi**

| Matching Directions | Mg Interatomic Spacing (nm) | AlNi Interatomic Spacing (nm) | Interatomic Misfit (pct) |
|---|---|---|---|
| $\langle 11\bar{2}0\rangle_{Mg}//\langle 111\rangle_{AlNi}$ | 0.320 | 0.249 | 22.2 |
| $\langle 11\bar{2}0\rangle_{Mg}//\langle 100\rangle_{AlNi}$ | 0.320 | 0.288 | 10.0 |
| $\langle 11\bar{2}0\rangle_{Mg}//\langle 110\rangle_{AlNi}$ | 0.320 | 0.407 | 27.2 |
| $\langle 10\bar{1}0\rangle_{Mg}//\langle 113\rangle_{AlNi}$ | 0.277 | 0.239 | 13.7 |
| $\langle 11\bar{2}3\rangle_{Mg}//\langle 113\rangle_{AlNi}$ | 0.305 | 0.239 | 21.6 |

**Table AIII. Calculated Interplanar Spacing for Mg and AlNi and Interplanar Spacing Mismatch Between Possible Matching Planes of Mg and AlNi**

| Matching Planes | Mg Interplanar Spacing (nm) | AlNi Interplanar Spacing (nm) | Interplanar Mismatch (pct) |
|---|---|---|---|
| $\{0002\}_{Mg}//\{110\}_{AlNi}$ | 0.260 | 0.204 | 21.5 |
| $\{10\bar{1}1\}_{Mg}//\{110\}_{AlNi}$ | 0.244 | 0.204 | 16.4 |
| $\{10\bar{1}0\}_{Mg}//\{110\}_{AlNi}$ | 0.277 | 0.204 | 26.3 |
| $\{0002\}_{Mg}//\{200\}_{AlNi}$ | 0.260 | 0.144 | 44.6 |
| $\{10\bar{1}1\}_{Mg}//\{200\}_{AlNi}$ | 0.244 | 0.144 | 41.0 |
| $\{10\bar{1}0\}_{Mg}//\{200\}_{AlNi}$ | 0.277 | 0.144 | 48.0 |
| $\{0002\}_{Mg}//\{111\}_{AlNi}$ | 0.260 | 0.166 | 36.1 |
| $\{10\bar{1}1\}_{Mg}//\{111\}_{AlNi}$ | 0.244 | 0.166 | 32.0 |
| $\{10\bar{1}0\}_{Mg}//\{111\}_{AlNi}$ | 0.277 | 0.166 | 40.1 |

Merwe's energy calculation, which was done along the close-packed directions between FCC and body-centered cubic (BCC).[22,24]

Identification of matching planes is the next step to predict the OR between Mg (HCP) and AlNi (BCC) crystal structure. These planes can be identified by calculation of structure factors or by looking at the powder X-ray diffraction intensities available from the published XRD databases. The biggest structure factor or the highest intensity of the X-ray diffraction corresponds to the closest-packed plane. In both HCP and BCC crystal structures, there are three close-packed or nearly close-packed planes (as shown in Table AI). Thus, there are nine possible plane pairs between HCP and BCC crystal structures. Table AIII shows the calculated results for the interplanar spacing mismatches between possible matching planes between Mg and AlNi.

To form an OR without large mismatch strain, the edge-to-edge matching model also requires a critical interplanar spacing mismatch value between matching planes, similar to the interatomic spacing misfit along matching directions. It has been reported that the approximate critical *d*-value mismatch is less than 6 pct, which is based on reported ORs in known systems.[25] Using 6 pct as the critical value, it can be concluded that there are no potential matching planes between Mg and AlNi (see Table AIII). Therefore, the formed OR between Mg and AlNi will have a high interplanar mismatch with large angle rotation of the matching planes (see Figures 7(d) and 11).

### *AlNi (BCC)-$Mg_2Ni$ (HCP) Interface (Mode I)*

The lattice parameters used in the current study are $a_H$ = 0.518 nm and $c_H$ = 1.319 nm for $Mg_2Ni$.[19] Table AIV shows the calculated results for the relative interatomic spacing misfits along possible matching directions between AlNi and $Mg_2Ni$. Table AV shows

**Table AIV. Interatomic Spacing Misfits Along Possible Matching Directions Between AlNi and $Mg_2Ni$**

| Matching Directions | AlNi Interatomic Spacing (nm) | $Mg_2Ni$ Interatomic Spacing (nm) | Interatomic Misfit (pct) |
|---|---|---|---|
| $\langle 111\rangle_{AlNi}//\langle 11\bar{2}0\rangle_{Mg_2Ni}$ | 0.249 | 0.518 | 108.0 |
| $\langle 100\rangle_{AlNi}//\langle 11\bar{2}0\rangle_{Mg_2Ni}$ | 0.288 | 0.518 | 79.9 |
| $\langle 110\rangle_{AlNi}//\langle 11\bar{2}0\rangle_{Mg_2Ni}$ | 0.407 | 0.518 | 27.3 |
| $\langle 113\rangle_{AlNi}//\langle 10\bar{1}0\rangle_{Mg_2Ni}$ | 0.239 | 0.449 | 87.9 |
| $\langle 113\rangle_{AlNi}//\langle 11\bar{2}3\rangle_{Mg_2Ni}$ | 0.239 | 0.622 | 160.2 |

**Table AV. Calculated Interplanar Spacing for AlNi and $Mg_2Ni$ and Interplanar Spacing Mismatch Between Possible Matching Planes of AlNi and $Mg_2Ni$**

| Matching Planes | AlNi Interplanar Spacing (nm) | $Mg_2Ni$ Interplanar Spacing (nm) | Interplanar Mismatch (pct) |
|---|---|---|---|
| $\{110\}_{AlNi}//\{0002\}_{Mg_2Ni}$ | 0.204 | 0.659 | 223.0 |
| $\{110\}_{AlNi}//\{10\bar{1}1\}_{Mg_2Ni}$ | 0.204 | 0.425 | 108.3 |
| $\{110\}_{AlNi}//\{10\bar{1}0\}_{Mg_2Ni}$ | 0.204 | 0.449 | 120.1 |
| $\{200\}_{AlNi}//\{0002\}_{Mg_2Ni}$ | 0.144 | 0.659 | 357.6 |
| $\{200\}_{AlNi}//\{10\bar{1}1\}_{Mg_2Ni}$ | 0.144 | 0.425 | 195.1 |
| $\{200\}_{AlNi}//\{10\bar{1}0\}_{Mg_2Ni}$ | 0.144 | 0.449 | 211.8 |
| $\{111\}_{AlNi}//\{0002\}_{Mg_2Ni}$ | 0.166 | 0.659 | 297.0 |
| $\{111\}_{AlNi}//\{10\bar{1}1\}_{Mg_2Ni}$ | 0.166 | 0.425 | 156.0 |
| $\{111\}_{AlNi}//\{10\bar{1}0\}_{Mg_2Ni}$ | 0.166 | 0.449 | 170.5 |

**Table AVI. Interatomic Spacing Misfits Along Possible Matching Directions Between $Mg_2Ni$ Phase and Ni Substrate**

| Matching Directions | $Mg_2Ni$ Interatomic Spacing (nm) | Ni Interatomic Spacing (nm) | Interatomic Misfit (pct) |
|---|---|---|---|
| $\langle 11\bar{2}0\rangle_{Mg_2Ni}//\langle 110\rangle_{Ni}$ | 0.518 | 0.249 | 51.9 |
| $\langle 11\bar{2}0\rangle_{Mg_2Ni}//\langle 100\rangle_{Ni}$ | 0.518 | 0.352 | 32.0 |
| $\langle 11\bar{2}0\rangle_{Mg_2Ni}//\langle 111\rangle_{Ni}$ | 0.518 | 0.610 | 17.8 |

the calculated interplanar spacings for AlNi and $Mg_2Ni$ and interplanar spacing mismatches. No potential matching direction was found between AlNi and $Mg_2Ni$ with $\delta$ less than the critical value of 10 pct (see Table AIV). Also, there are no potential matching planes between AlNi and $Mg_2Ni$ with interplanar spacing mismatch less than the critical value of 6 pct (see Table AV). These lead to a large angle rotation of the matching planes with high interplanar mismatch between AlNi and $Mg_2Ni$ (see Figure 8).

### *$Mg_2Ni$ (HCP)-Ni (FCC) Interface (Mode I)*

In FCC crystal structures, there are three close-packed or nearly close-packed directions (all straight atom rows) and three close-packed or nearly close-packed planes (see Table AI). With this assumption that the Ni (FCC) is the parent phase (substrate), and $Mg_2Ni$ phase (HCP) is formed on the substrate as the product, Table AVI shows the calculated interatomic spacings for $Mg_2Ni$ and Ni and interatomic misfits along possible matching directions (all pairs are straight) between them ($a_F$ = 0.352 nm for Ni[19]). Calculated results (Table AVI) show that there are no potential matching directions with the interatomic spacing misfit less than the critical value of 10 pct between the Ni-electroplated layer and the $Mg_2Ni$ phase at the interface. Table AVII shows the calculated results for the interplanar spacing mismatches between possible matching planes between $Mg_2Ni$ phase and Ni. Using 6 pct as the critical value, it can be concluded that there are no potential matching planes between $Mg_2Ni$ and Ni (see Table AVII), and, therefore, a large angle rotation of matching planes with high interplanar mismatch forms between $Mg_2Ni$ and Ni (see Figure 9(c)).

### *AlNi (BCC)-Fe (BCC) Interface (Mode II)*

The lattice parameter used for Fe was 0.286 nm.[19] With the assumption that Fe is the substrate and AlNi is the formed phase (product), Tables AVIII and AIX show the calculated results for the relative interatomic spacing misfits and interplanar spacing mismatches between Fe and AlNi, respectively. The interatomic spacing misfits less than the critical value of 10 pct between the AlNi phase and Fe substrate at the interface were found along $\langle 111\rangle_{Fe}//\langle 111\rangle_{AlNi}$, $\langle 100\rangle_{Fe}//\langle 100\rangle_{AlNi}$, $\langle 110\rangle_{Fe}//\langle 110\rangle_{AlNi}$, and $\langle 113\rangle_{Fe}//\langle 113\rangle_{AlNi}$ (see Table AVIII). Also, the interplanar spacing mismatches less than the critical value of 6 pct are for $\{110\}_{Fe}//\{110\}_{AlNi}$, $\{200\}_{Fe}//\{200\}_{AlNi}$, and $\{111\}_{Fe}//\{111\}_{AlNi}$ (see Table AIX). The plane pair of $\{110\}_{Fe}//\{110\}_{AlNi}$

**Table AVII. Calculated Interplanar Spacing for $Mg_2Ni$ Phase and Ni Substrate and Interplanar Spacing Mismatch Between Possible Matching Planes of $Mg_2Ni$ and Ni**

| Matching Planes | $Mg_2Ni$ Interplanar Spacing (nm) | Ni Interplanar Spacing (nm) | Interplanar Mismatch (pct) |
|---|---|---|---|
| $\{0002\}_{Mg_2Ni}//\{111\}_{Ni}$ | 0.659 | 0.203 | 69.2 |
| $\{0002\}_{Mg_2Ni}//\{110\}_{Ni}$ | 0.659 | 0.249 | 62.2 |
| $\{0002\}_{Mg_2Ni}//\{100\}_{Ni}$ | 0.659 | 0.352 | 46.6 |
| $\{10\bar{1}1\}_{Mg_2Ni}//\{111\}_{Ni}$ | 0.425 | 0.203 | 52.2 |
| $\{10\bar{1}1\}_{Mg_2Ni}//\{110\}_{Ni}$ | 0.425 | 0.249 | 41.4 |
| $\{10\bar{1}1\}_{Mg_2Ni}//\{100\}_{Ni}$ | 0.425 | 0.352 | 17.2 |
| $\{10\bar{1}0\}_{Mg_2Ni}//\{111\}_{Ni}$ | 0.449 | 0.203 | 54.8 |
| $\{10\bar{1}0\}_{Mg_2Ni}//\{110\}_{Ni}$ | 0.449 | 0.249 | 44.5 |
| $\{10\bar{1}0\}_{Mg_2Ni}//\{100\}_{Ni}$ | 0.449 | 0.352 | 21.6 |

**Table AVIII. Interatomic Spacing Misfits Along Possible Matching Directions Between AlNi Phase and Fe Substrate**

| Matching Directions | AlNi Interatomic Spacing (nm) | Fe Interatomic Spacing (nm) | Interatomic Misfit (pct) |
|---|---|---|---|
| $\langle 111\rangle_{AlNi}//\langle 111\rangle_{Fe}$ | 0.249 | 0.248 | 0.4 |
| $\langle 100\rangle_{AlNi}//\langle 111\rangle_{Fe}$ | 0.288 | 0.248 | 13.9 |
| $\langle 110\rangle_{AlNi}//\langle 111\rangle_{Fe}$ | 0.407 | 0.248 | 39.1 |
| $\langle 111\rangle_{AlNi}//\langle 100\rangle_{Fe}$ | 0.249 | 0.286 | 14.8 |
| $\langle 100\rangle_{AlNi}//\langle 100\rangle_{Fe}$ | 0.288 | 0.286 | 0.7 |
| $\langle 110\rangle_{AlNi}//\langle 100\rangle_{Fe}$ | 0.407 | 0.286 | 29.7 |
| $\langle 111\rangle_{AlNi}//\langle 110\rangle_{Fe}$ | 0.249 | 0.404 | 62.2 |
| $\langle 100\rangle_{AlNi}//\langle 110\rangle_{Fe}$ | 0.288 | 0.404 | 40.3 |
| $\langle 110\rangle_{AlNi}//\langle 110\rangle_{Fe}$ | 0.407 | 0.404 | 0.7 |
| $\langle 113\rangle_{AlNi}//\langle 113\rangle_{Fe}$ | 0.239 | 0.237 | 0.8 |

**Table AIX. Calculated Interplanar Spacing for AlNi Phase and Fe Substrate and Interplanar Spacing Mismatch Between Possible Matching Planes of AlNi and Fe**

| Matching Planes | AlNi Interplanar Spacing (nm) | Fe Interplanar Spacing (nm) | Interplanar Mismatch (pct) |
|---|---|---|---|
| $\{110\}_{AlNi}//\{110\}_{Fe}$ | 0.204 | 0.202 | 1.0 |
| $\{200\}_{AlNi}//\{110\}_{Fe}$ | 0.144 | 0.202 | 40.3 |
| $\{111\}_{AlNi}//\{110\}_{Fe}$ | 0.166 | 0.202 | 21.7 |
| $\{110\}_{AlNi}//\{200\}_{Fe}$ | 0.204 | 0.143 | 29.9 |
| $\{200\}_{AlNi}//\{200\}_{Fe}$ | 0.144 | 0.143 | 0.7 |
| $\{111\}_{AlNi}//\{200\}_{Fe}$ | 0.166 | 0.143 | 13.8 |
| $\{110\}_{AlNi}//\{111\}_{Fe}$ | 0.204 | 0.165 | 19.1 |
| $\{200\}_{AlNi}//\{111\}_{Fe}$ | 0.144 | 0.165 | 14.6 |
| $\{111\}_{AlNi}//\{111\}_{Fe}$ | 0.166 | 0.165 | 0.6 |

contains all the possible matching direction with small misfit values, but plane pair of $\{200\}_{Fe}//\{200\}_{AlNi}$ only contains $\langle 100\rangle_{Fe}//\langle 100\rangle_{AlNi}$ and $\langle 110\rangle_{Fe}//\langle 110\rangle_{AlNi}$ direction pairs and the plane pair of $\{111\}_{Fe}//\{111\}_{AlNi}$ just contains $\langle 110\rangle_{Fe}//\langle 110\rangle_{AlNi}$ direction pair. Therefore, these combinations of plane pairs and the direction pairs have the potential to form an OR. These conditions lead to a low angle rotation of the lattice planes along the matching directions and a low mismatch strain at the interface of Fe and AlNi (see Figure 13).

## REFERENCES


1. G. Bailey and H. Watkins: *J. Inst. Met.*, 1952, vol. 80, pp. 57–76.
2. G. Kumar and K.N. Prabhu: *Adv. Colloid Interface Sci.*, 2007, vol. 133, pp. 61–89.
3. A.M. Nasiri, P. Chartrand, D.C. Weckman, and Y. Zhou: *Metall. Mater. Trans. A*, 2013, vol. 44A, pp. 1937–46.
4. N. Eustathopoulos: *Acta Mater.*, 1998, vol. 46, pp. 2319–27.
5. I. Aksay, C. Hoye, and J. Pask: *J. Phys. Chem.*, 1974, vol. 78, pp. 1178–83.
6. N. Eustathopoulos and B. Drevet: *J. Phys. III*, 1994, vol. 4, pp. 1865–81.
7. E. Saiz, C.W. Hwang, K. Suganuma, and A.P. Tomsia: *Acta Mater.*, 2003, vol. 51, pp. 3185–97.
8. L.B. Freund and S. Suresh: *Thin Film Materials, Stress, Defect Formation and Surface Evolution*, University Press, Cambridge, 2003.
9. M.E. Glicksman: *Principles of Solidification*, Springer Science + Business Media, LLC 2011, DOI:10.1007/978-1-4419-7344-3_12 .
10. L.M. Liu: *Welding and Joining of Magnesium Alloys*, Woodhead Publishing Limited, Cambridge, 2010.
11. N. Eustathopoulos, M.G. Nicholas, and B. Drevet: *Wettability at High Temperatures,* Pergamon Materials Series, Oxford, 1999, p. 187, 202, 399.
12. R. Voitovitch, A. Mortensen, and N. Eustathopoulos: *Acta Mater.*, 1999, vol. 47, pp. 1117–28.
13. O. Dezellus, F. Hodaj, and N. Eustathopoulos: *Acta Mater.*, 2002, vol. 47, pp. 4741–53.

14. A.M. Nasiri, D.C. Weckman, and Y. Zhou: *Weld. J.*, 2013, vol. 92, pp. 1–10.
15. Material Safety Data Sheet 2003, Superior Flux & Mfg. Co., November 11.
16. T.M. Moore: *Microsc. Today*, 2005, vol. 13, p. 40.
17. N.A. Belov, D.G. Eskin, and N.N. Avxentieva: *Acta Mater.*, 2005, vol. 53, pp. 4709–22.
18. A. Gasparyan and A. Shteinberg: *Combus. Explos. Shock Waves*, 1988, vol. 24, pp. 324–30.
19. W.B. Pearson: *Lattice Spacings and Structures of Metals and Alloys*, Pergamon Press, New York.
20. E. Abe, Y. Kawamura, K. Hayashi, and A. Inoue: *Acta Mater.*, 2002, vol. 50, pp. 3845–57.
21. D. Turnbull and R. Vonnegut: *Ind. Eng. Chem.*, 1952, vol. 44, pp. 1292–98.
22. M.X. Zhang and P.M. Kelly: *Acta Mater.*, 2005, vol. 53, pp. 1073–84.
23. M.X. Zhang and P.M. Kelly: *Acta Mater.*, 2005, vol. 53, pp. 1085–96.
24. J.H. van der Merwe: *Phil. Mag. A*, 1982, vol. 45, pp. 127–43.
25. D. Duly: *Acta Metall. Mater.*, 1993, vol. 41, pp. 1559–66.